Modeling and Testing of 9m Research Blades*

Joshua Paquette†, Daniel Laird‡, and D. Todd Griffith§
*Sandia National Laboratories**, *Albuquerque, NM, 87185, USA*

Laura Rip
National Renewable Energy Laboratory, Golden, CO, 80401, USA

Wind turbines and their blades continue to grow in size. The resulting increase in blade mass and cost requires the implementation of new design concepts. Among these is the selective use of carbon fiber. In 2002, Sandia National Laboratories (SNL) initiated a research program to investigate the use of carbon fiber in 9m subscale blades. Two sets of blades were designed, one with a carbon spar-cap and the other with off-axis carbon in the skin which produces bend twist coupling. Blades of each design have recently undergone modal and structural testing. In addition, finite element analysis (FEA) of both blades has been performed. This paper describes the design, testing, and analysis work that have been completed.

Nomenclature

SNL	=	Sandia National Laboratories
NREL	=	National Renewable Energy Laboratory
GEC	=	Global Energy Concepts
TPI	=	TPI Composites
FRF	=	Frequency Response Function
FEA	=	Finite Element Analysis

I. Introduction

IN 2002, Sandia National Laboratories (SNL) initiated a research program to demonstrate the use of carbon fiber in subscale blades. At that time, carbon was not being utilized in commercial blades. This research effort had many goals, one of which was to demonstrate the use of carbon in a predominantly glass wind turbine blade. Other goals were to design and fabricate a bend-twist coupled blade, validate design and analysis tools, and demonstrate new testing methods. Analytical studies of bend-twist coupling concepts have been performed by researchers at Sandia and elsewhere.[1,2,3,4,5]

This research effort has produced two sets of 9m blades. The first set of blades, named CX-100, has a carbon spar cap infused with the rest of the blade as part of the normal glass blade fabrication process. The second set of blades, named TX-100, has a glass spar cap but utilizes off-axis carbon fiber in the skin of the blade to produce bend-twist coupling. The fabrication of these blades was completed by TPI Composites in early 2005.

Laboratory testing of CX-100 and TX-100 blades has been performed at both SNL and National Renewable Energy Laboratory (NREL). Modal testing of the blade sets has been performed at SNL while the static testing of the blades was performed at the NREL.

Basic finite element models of both the CX-100 and TX-100 blades have been generated using the NuMAD[6,7,8] code developed at SNL. In an effort to quantify element formulation limitations discussed previously[9], the finite element models were generated with both offset-node, layered shell elements and layered solid elements. Both

† Member of the Technical Staff, Wind Energy Technology Department, MS-0708
‡ Principal Member of the Technical Staff, Wind Energy Technology Department, MS-0708
§ Structural Dynamics Research Department, MS-0196
** Sandia is a multiprogram laboratory operated by Sandia Corporation, a Lockheed Martin Company, for the U.S. Department of Energy under contract DE-AC04-94AL85000.

modal and static structural analysis was conducted. These predictions were then compared to the available testing results.

II. Blade Designs

Through a contract funded by SNL, three different blades designs were collaboratively generated by Global Energy Concepts[10] (GEC), MDZ consulting, and TPI Composites, Inc.[11] (TPI). This effort included the design of a baseline fiberglass blade, a carbon-glass hybrid blade of conventional design, and a twist-coupled carbon-glass hybrid design. All designs were 9 meters in length with the same external geometry.

The baseline fiberglass blade design was generated for comparison purposes only (paper blade) and was given the designation "GX-100" for G(lass e)X(perimental) 100(kw). All blade designs were generated for a 20-year life per IEC Class 2 loads with turbulence level "B."

The carbon-glass hybrid blade of conventional design, CX-100, utilizes a spar of unidirectional carbon fibers running along the blade span. A schematic of the CX-100 is shown in Figure 1. The carbon spar cap begins at the root and extends for nearly the entire length of the blade (9m). Figure 2 shows the internal surface of a high-pressure side of the blade. Compared to the GX-100, the CX-100 design resulted in a mass reduction of approximately 50% in the blade spar. However, because the baseline GX-100 fiberglass skins are a substantial fraction of the total blade weight, the overall mass reduction in the CX-100 was limited to approximately 11%. In addition, the CX-100 is substantially stiffer than the GX-100, resulting in a 70% increase in tip/tower clearance margin.

The twist-coupled carbon-glass hybrid design, TX-100, utilizes a fiberglass spar and outboard carbon skins (Figure 1). The fibers in the carbon skins are off-axis to achieve twist-bend coupling (Figure 3). An earlier study had indicated that for this size blade (9m), bend-twist coupling would be maximized by using the carbon in the skin rather than in the spar cap[12]. This general type of design is called "passively adaptive" because the blade will twist to reduce loads (adaptive) but no activation energy is required (passive).

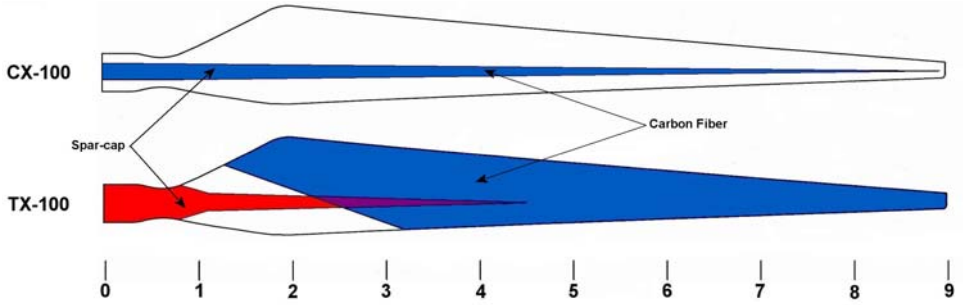

Figure 1. Schematic drawings of CX-100 and TX-100 blades.

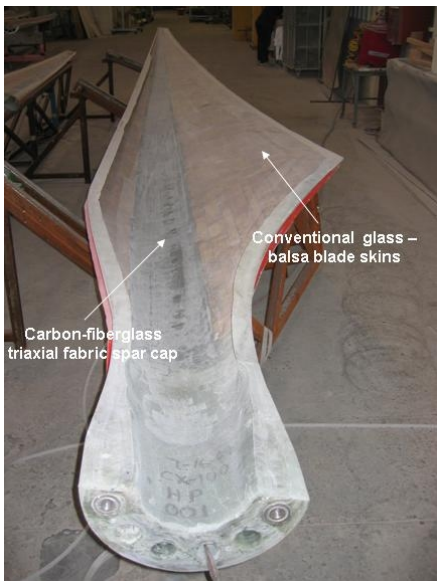

Figure 2. CX-100 high-pressure skin.

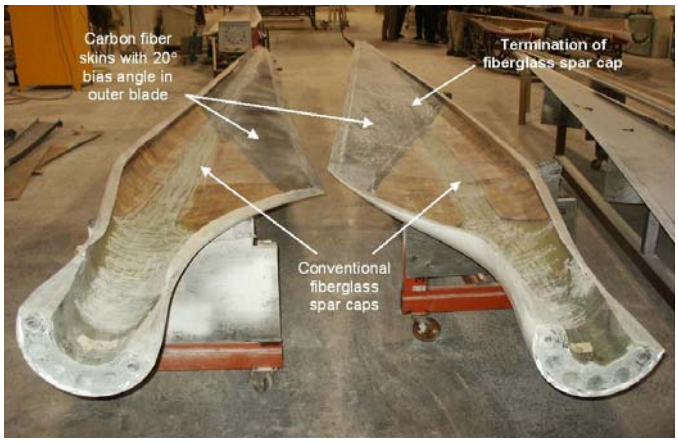

Figure 3. TX-100 high-pressure and low-pressure skins.

III. Experimental Setup

Laboratory testing of CX-100 and TX-100 blades was performed at both SNL and the NREL. Modal testing of the blade sets was performed at SNL and static tests were performed at NREL.

A. Modal Test Description

Several important factors considered in the test setup were the suspension method, protection of the blade surface, instrumentation, environmental factors, and mass loading effects.

Each blade was tested in a free-free condition because this is both practical to implement and suitable for model validation. Any other constraint condition is affected by the compliance of the system. For instance, if the blade were to be tested while mounted at the hub, the compliance of the mount would affect the results and thus, the mount would also need to be characterized in the model. Therefore, special care must be taken so that the suspension system does not have a significant effect on the measured frequency and damping values. For these tests, the blade was supported by nylon straps and was dynamically isolated using bungee cords. Additionally, it should be noted that the fragile trailing edge of the blade cannot withstand a highly concentrated load; therefore the blade was suspended with the leading edge down.

The blades were tested in two configurations. First, the blade was suspended at two locations using two independent tripods positioned fore and aft the blade's center of gravity (CG). At each location, the blade was supported by a single nylon strap which was linked to the tripod with a coil of bungee rope. The double strap suspension configuration is shown in Figure 4. In order to evaluate the suspension setup, tests were repeated for a different suspension configuration using only a single nylon strap and tripod positioned at the CG as shown in Figure 5. Frequency response functions (FRF) from the two configurations were observed, and the frequency differences between the single and double strap tests were found to be minimal. Additionally, there was adequate frequency separation between rigid body modes related to the suspension and the first flexible blade mode in line with the bungees[13]. If inadequate frequency separation between the suspension and blade modes were to occur, it would have been possible to reduce the stiffness of the coiled bungee rope by reducing the number of turns of the rope used to support the blade.

Figure 4. Double strap suspension configuration.

Figure 5. Single strap suspension configuration.

The instrumentation of an individual blade consisted of 68 accelerometers rated at 50 g's, mounted in pairs at the 34 locations shown in Figure 6. Accelerations were measured in both the x-direction (flapwise) and z-direction (edgewise) while acceleration in the y-direction (axial) was neglected. All the accelerometers were oriented with no more than 3 degree error for all three axes as determined by a digital inclinometer.

The structure was excited using a 3 lb impact hammer. Nine data sets were acquired for each blade corresponding to nine different force excitation locations. Excitation in the x-direction was performed near the pitch axis and near the trailing edge at the stations defined by accelerometer positions 131-133, 141-143, and 161-163 as seen in Figure 6. In this way, both flap and torsional modes were excited. Excitation in the z-direction was performed at the leading edge of the previously mentioned stations to obtain edgewise modes.

These tests were conducted an uncontrolled temperature environment. The temperatures for the CX-100 test ranged from 34 to 50°F and from 72 to 83°F for the TX-100 tests. For both sets of tests, FRF's were compared and it was determined that the temperature variation had a small effect on the measured frequencies.

Mass loading effects of the accelerometers were studied. Proper identification of mode shapes requires an adequate number of accelerometers for providing the required spatial resolution to identify a particular mode shape. This can come at a cost as increased spatial resolution in the measurements requires more mass to be loaded onto the structure being tested. As mentioned previously, the test setup utilized 68 accelerometers. In order to characterize the mass loading effect, all but four accelerometers were removed and the blade was tested once again. The results showed a small but noticeable difference in the frequencies between the two setups. Thus, the natural frequency and damping values reported are those taken from the lightly instrumented blade while the experimentally determined mode shapes used to compare with the analysis are from the fully instrumented blade data.

B. Static Test Description

Static flap-bending tests of the CX-100 and TX-100 blades were conducted at NREL. Photographs of the blades mounted in the test fixture are shown in Figure 7 and Figure 8. The blades were loaded using a three point wiffle-tree arrangement. The loading locations were optimized to provide a close approximation of the desired test-moment distribution. For these tests, loads were applied at 3.00, 5.81, and 7.62 m locations. The load was applied to the blades through the use of saddles which conformed to the profile of the airfoil at the station where they were located. Loading was applied to the blades at their pitch axes. For the TX-100 test, a pulley and cable arrangement as seen in Figure 8 was used in an attempt to keep the loading point constant while allowing the blade to rotate freely.

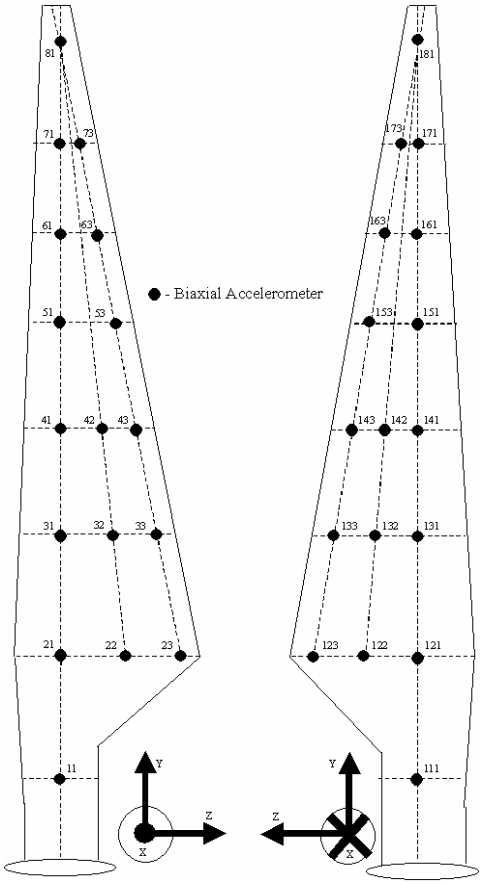

Figure 6. Accelerometer locations.

Figure 7. CX-100 blade in test fixture.

Figure 8. TX-100 blade in test fixture.

The CX-100 blade was instrumented with string pots at the trailing edge of each saddle location and strain gauges located as shown in Figure 9. A load cell was attached to the hoist which applied the load. The strain gauges were placed along the spar cap on both sides of the blade, at the root, and at two locations where panel buckling was thought to be probable.

The TX-100 blade was instrumented with string pots at the leading and trailing edges of the blade at the 3 m and 5.81 m stations, and at the trailing edge of the 7.26 m station. Additionally, accelerometers were located at 4.3, 6.25 and 7.95 m stations. The added string pots and accelerometers were used to measure twist in the blade upon flap loading. Similar strain-gauging was used on the TX-100 blade with the exception of the two outboard most gauges being eliminated.

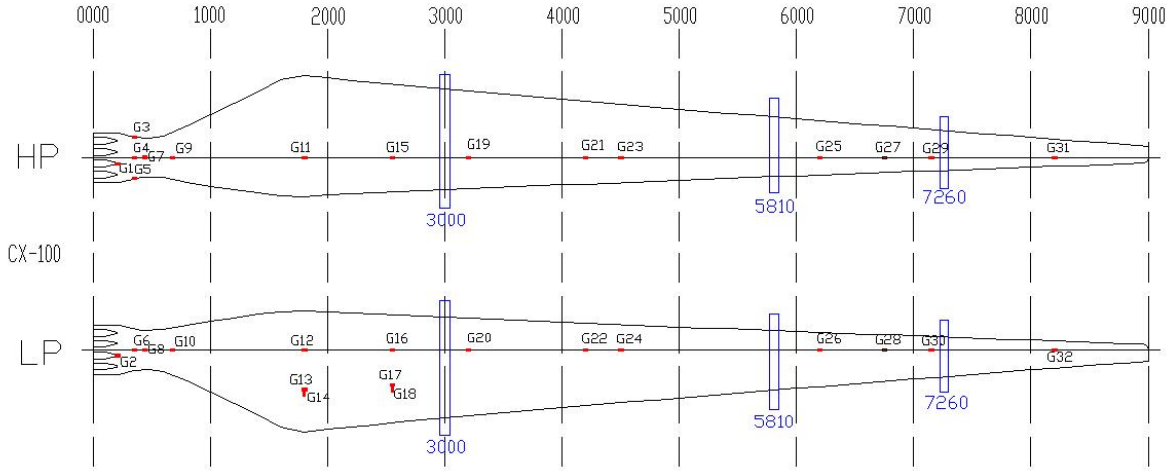

Figure 9. Strain gauge and saddle locations for CX-100 blade (dimensions in mm).

Since the load was to be applied vertically from the ceiling of the test facility, the fixture to which the blade was attached was rotated in two directions to best simulate the loading seen in operation. The blade was rotated 5.25° about its pitch axis to reflect operating conditions. Additionally, the tip was rotated down so that at the 100% test load, the forces would be applied perpendicular to the blade surface as shown in Figure 10.

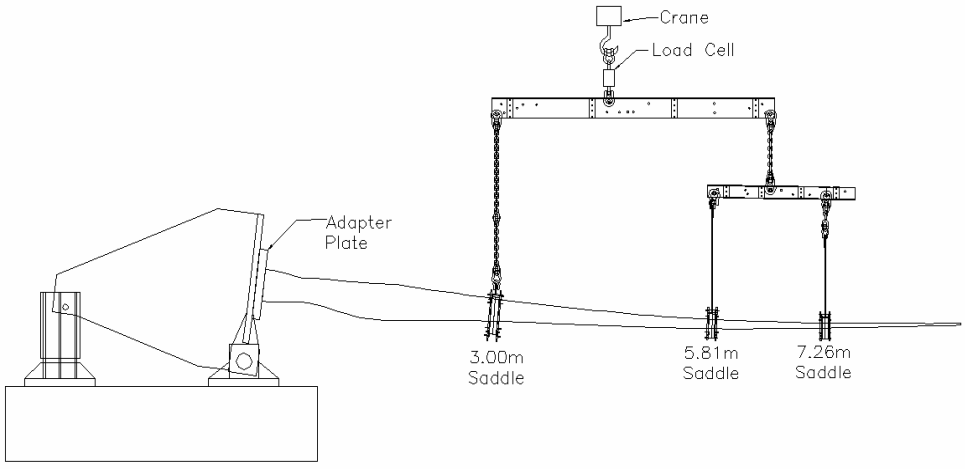

Figure 10. Drawing of blade in test fixture at 100% test load.

The blade was loaded and unloaded in a stepped sequence (see Figure 11) in progressively higher amounts up to a predefined 100% test load. After obtaining the 100% test load, the blade was to be unloaded, loaded to 110%, and then stepped in 10% increments until failure occurred. The test load was calculated by multiplying the design load by a factor of 1.1. The design load for the CX-100 blade was based on peak loading event in IEC Class 2 loads with turbulence level "B" along with a partial safety factor of 1.35. The resulting moment distribution in the blade at the test load is shown in Figure 12, along with the moment distribution resulting from the design load. This test load

distribution is achieved with 6286 lb applied to the wiffle-tree. For the TX-100 blade, it was realized that this design criterion would constrain aero-elastic twist. Thus the event of a peak 50-year load with the blades fully feathered was removed as a design constraint. The resulting design and test moment distributions for the TX-100 blade are shown in Figure 13. This test load distribution is achieved with 3457 lb applied to the wiffle-tree.

It should be noted that due to a manufacturing defect, the blade that was originally scheduled to undergo static testing was feared to have a reduction in aero-elastic twist. Thus another blade that that did not have the defect also underwent static testing. It was a blade that was also scheduled to be field tested and thus could not be damaged. Taking this into consideration, this blade was only loaded up to 67% of the test load. All displacement, strain, and rotation results quoted are from this blade. The original test blade, which contained the defect, was loaded until failure.

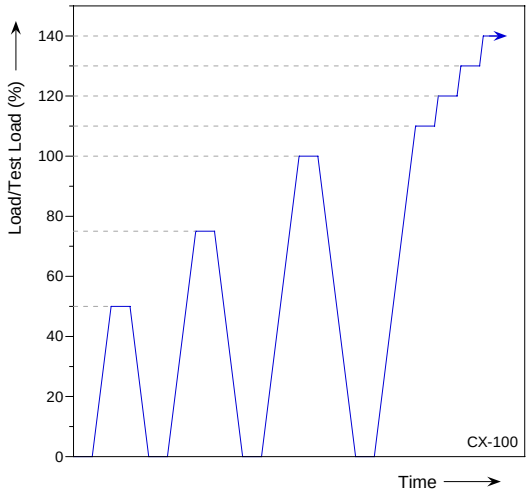

Figure 11. CX-100 static test loading sequence.

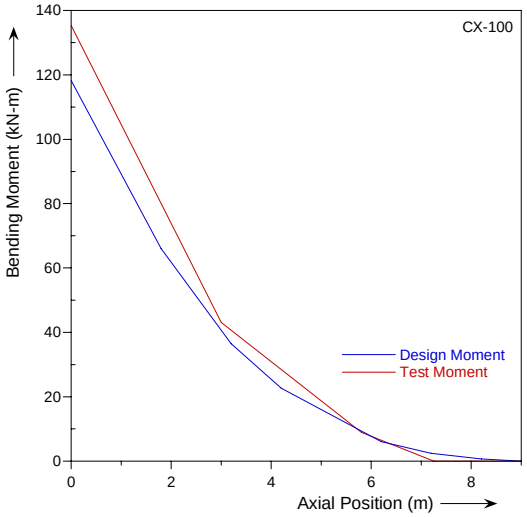

Figure 12. CX-100 design and test moment distributions.

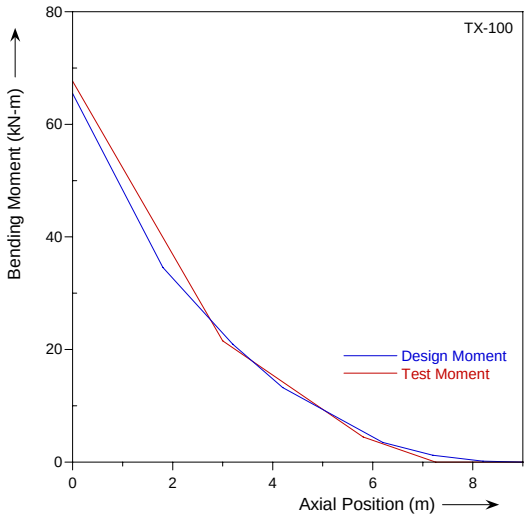

Figure 13. TX-100 design and test moment distributions.

IV. Experiment Results

The data from the modal tests was used to generate frequency, damping, and mode shape data for the CX-100 and TX-100 blades. Static testing produced strain and deflection data for the two blades in response to a flapwise bending load.

A. Modal Test Results

The frequency and damping results for the first five modes from the CX-100 and TX-100 experiments performed at SNL are given in Table 1 and Table 2 respectively. The description of each mode was determined by viewing the experimental mode shapes and comparing them with the theoretical mode-shapes for a free-free beam[14]. The five modes listed complete a baseline set of modes up to 50 Hz for comparison of the experimental and analytical models. Also, the number of uniformly distributed span-wise accelerometer mounting locations (eight in total) offered excellent spatial resolution to identify the modes shown in Tables 1 and 2.

Table 1. Frequency, damping, and mode shape correlation for the first five modes from CX-100 experiments.

Mode Description	CX-100 #002		CX 100 #006		MAC Correlation (%)
	Frequency (Hz)	Damping (%)	Frequency (Hz)	Damping (%)	
1st Flap	7.99	1.11	7.97	2.44	95.4
1st Edge	17.18	1.58	17.15	1.94	98.9
2nd Flap	20.35	1.53	20.24	1.87	99.4
3rd Flap	34.10	0.83	33.80	1.20	94.9
2nd Edge	44.38	0.71	44.87	1.22	99.8

Table 2. Frequency, damping, and mode shape correlation for the first five modes from TX-100 experiments.

Mode Description	TX-100 #002		TX 100 #006		MAC Correlation (%)
	Frequency (Hz)	Damping (%)	Frequency (Hz)	Damping (%)	
1st Flap	6.44	0.27	6.49	0.20	97.0
2nd Flap	15.16	0.26	15.14	0.23	98.0
1st Edge	25.00	0.32	25.25	0.34	97.5
3rd Flap	28.44	0.31	28.94	0.60	98.0
4th Flap	43.89	0.37	43.92	0.34	94.9

A standard tool in modal analysis is the Modal Assurance Criterion (MAC). Essentially, MAC provides a correlation metric between two sets of mode-shape vectors, and is defined mathematically as

$$MAC_{ij} = \frac{\left(\phi_i^T \psi_j\right)^2}{\left(\phi_i^T \phi_j\right)\left(\psi_i^T \psi_j\right)}$$

where ϕ and ψ are the shape vectors to be compared. The result of a MAC analysis is a matrix containing correlation values ranging from 0 to 1. Correlations of 90% or better are considered to be very good. A sample MAC analysis of the mode shape vectors for the two TX-100 blades is represented graphically in Figure 14. The high values on the diagonal reflect the strong correlation between mode shapes found between the two blades. This is also displayed in the small variation in frequency and damping values seen in Table 2. The MAC correlation values for the two sets of tests are given in Table 1 and Table 2

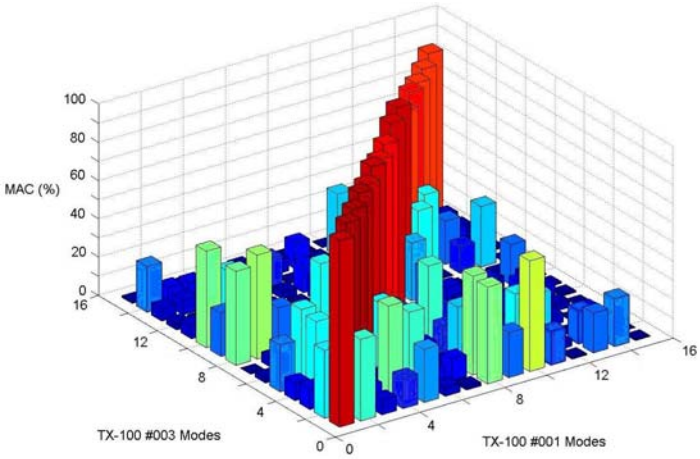

Figure 14. Sample MAC analysis of the experimental modal results from the two TX-100 blade specimens.

These results indicate that within each set of tests, the blades were very similar in terms of frequency, damping, and shape. The CX-100 blade is seen to have higher frequencies for flap modes and lower frequencies for edge modes as compared to the TX-100 blade. This indicates that the CX-100 blade is stiffer in the flapwise direction but more compliant in the edgewise direction.

B. Static Test Results

Figure 15 shows the deflection of the CX-100 blade when subjected to the 100% test load. The deflected shape shown was calculated using the string-pot data taken during the experiment along with the fixed boundary condition present at the root end. The blade is seen to have had a tip deflection of 1.03 m.

In Figure 16, the strains along the center of the spar cap for both the high-pressure and low-pressure surfaces of the blade at the 100% test load are plotted. The maximum strain was 0.3% and occurred at the 4.5 m station. Another strain peak occurred at the 0.675 m station which was the end of the root build-up for this blade.

The CX-100 blade failed at 107% of the test load due to panel buckling between the 1 m and 2 m stations aft of the leading edge. A detailed investigation will be performed in the future to determine the exact cause of the failure.

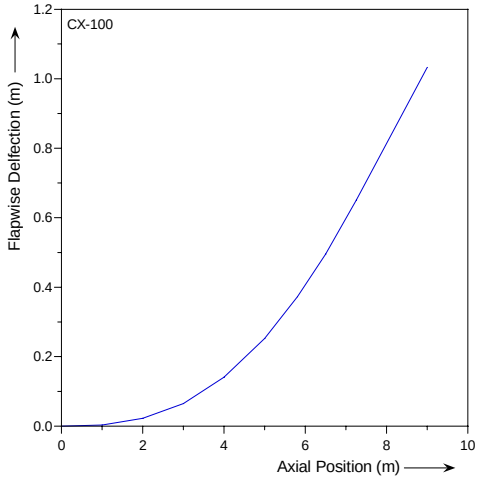

Figure 15. Deflected shape of the CX-100 blade at 100% test load.

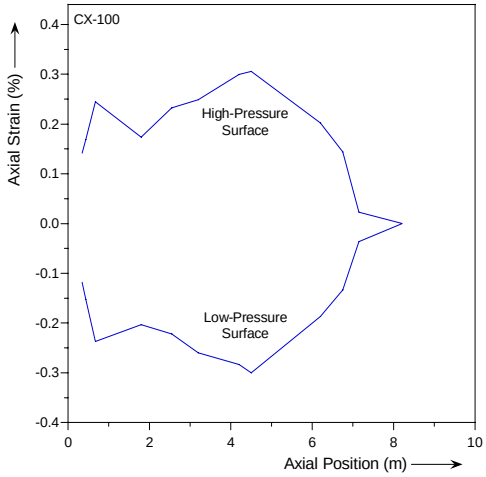

Figure 16. Strains along the center of the spar-cap for the CX-100 blade at 100% test load.

Figure 17 shows the deflection of the TX-100 blade at the 67% test load. The deflected shape shown was calculated in the same manner as for the CX-100 blade. The TX-100 blade is seen to have had a tip deflection of 0.74 m.

In Figure 18, the strains along the center of the spar cap for both the high-pressure and low-pressure surfaces of the blade at the 67% test load are plotted. The maximum strain was 0.22% and occurred at the 4.7 m station on the low-pressure surface of the blade. This point is just outboard of the end of the spar cap. This strain peak was not observed on the high-pressure surface. However, due to manufacturing uncertainties, the high-pressure and low-pressure spar caps may not have ended at exactly the same point. Thus it is possible that the gauge location on the high-pressure side of the blade was poorly positioned to capture this local phenomenon.

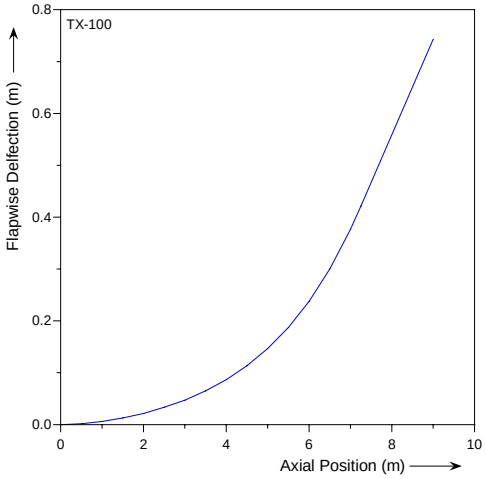

Figure 17. Deflected shape of the TX-100 blade at 67% test load.

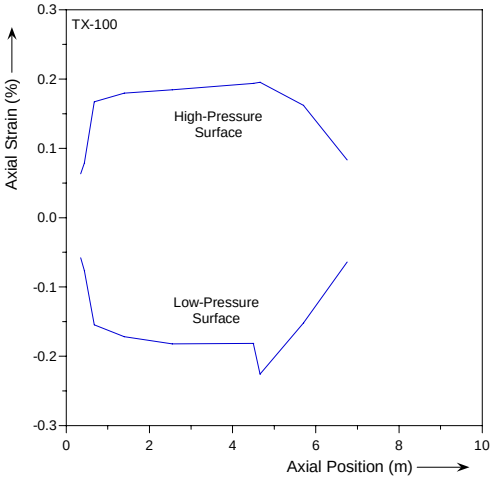

Figure 18. Strains along the center of the spar-cap for the TX-100 blade at 67% test load.

Figure 19 shows the rotation that was measured in the TX-100 blade upon flap loading to the 67% test load. The maximum rotation of -2.1° is seen to occur at the 6.1 m station. This result should be viewed with suspicion as it was observed that the cable and pulley system used did not rotate as freely as had been hoped and thus may have put an unknown torque on the blade.

The TX-100 blade failed at 180% of the test load due to a catastrophic fracture at approximately the 1 m station on the low-pressure side. Further investigation of the failure of this blade will be performed in the future.

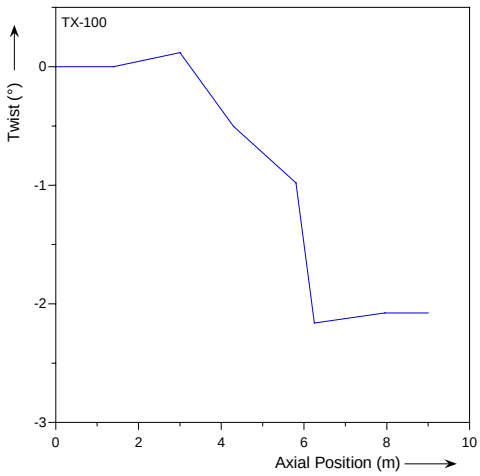

Figure 19. Rotation of the TX-100 blade at 67% test load.

V. Analysis

Finite element analysis (FEA) models were generated and analyzed in ANSYS[15] and compared against the experimental results from the modal and structural tests. The models were created using the NuMAD code developed at SNL.

A. Model Development and Analysis

Two FEA models of each blade were constructed consisting of approximately 13,000 elements. One model consisted of 8-node, layered shell elements (SHELL99) with mid-thickness nodes for the shear web and offset nodes for the skin. The other model used 20-node, layered bricks (SOLID191) instead of shells for the skin elements only. The brick model was created by offsetting the shell model so that the two models would have a similar number of elements and similar element geometries. Cross-sections from the two types of models are shown in Figure 20. The two different models were created to examine the effect of using offset-node shell elements which has been found to be potentially problematic when shearing deformations are present[9]. The TX-100 design uses off-axis fibers in the skin to couple flap-bending with twisting and thus exhibits shear deformation under aerodynamic loading. A plot of the CX-100 and TX-100 blade models is shown in Figure 21. In this figure, the material constant sets have been displayed in color to highlight the different lay-ups that comprise the two blades. Note the full-length spar-cap on the CX-100 and the diagonal division on the TX-100 model signifying the boundary of the off-axis carbon fiber region.

Initially, the models were found to be about 20% deficient in mass from what was measured on the manufactured blades. This discrepancy in the model is believed to have been caused by a variety of factors including uncertainty in the fiber volume fraction, and the absence of internal flanges, excess bonding agent, and root carrots which are all found in the as-built blade. To partially remedy this, point masses were added to the model to represent the mass of the root carrots. It was

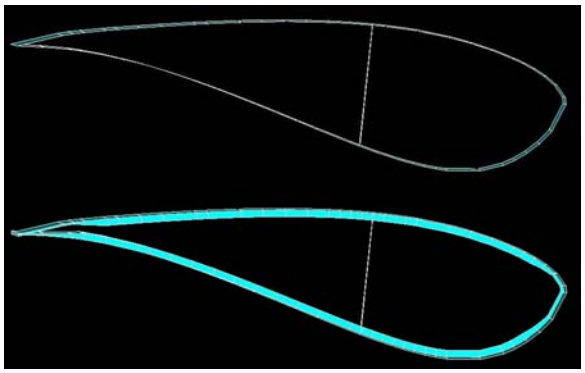

Figure 20. Cross-sections from shell (top) and brick (bottom) FEA models.

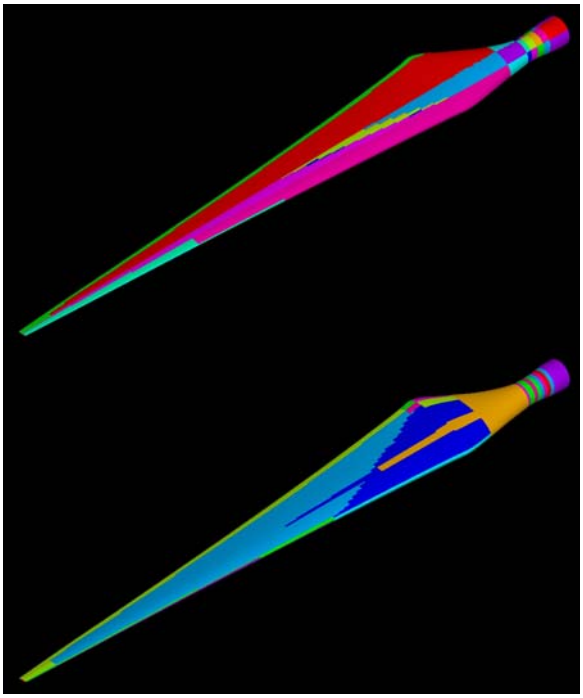

Figure 21. Plots of FE models of CX-100 (top) and TX-100 (bottom) blades showing areas of differing material constants.

decided that this would be the extent of the modifications as the root carrots were the only part of the missing mass for which both the magnitude and position were known with certainty. The addition of the root carrots was found to have a minimal effect on the modes being investigated.

An unconstrained modal analysis was completed on each model to correspond to the experiments. Upon completion of the analysis, the results were interrogated and all rigid body modes were excluded. From the remaining results, nodes were selected from the model whose locations most closely matched those of the accelerometers used in the experiments. The flapwise and edgewise deflections of these nodes were extracted and put into a suitable vector format, and a MAC analysis was performed between the experimental and analytical mode shapes.

B. Modal Analysis Results

Table 3 and Table 4 give descriptions of the first five modes found in the analysis of each blade/model configuration and their frequencies. The frequencies of the experimentally found modes of the same description are also given for reference. In addition, the MAC correlation values comparing the shell and brick models to the experiments and the shell models to the brick models are listed. The experimental values are averaged between the two blades.

Table 3. Comparison of experimental and FEA modal results for CX-100.

Description	Frequency (Hz)			MAC Correlation (%)		
	Shell Model	Brick Model	Test (Avg.)	Shell Model-Test (Avg.)	Brick Model-Test (Avg.)	Shell Model-Brick Model
1st Flap	8.52	8.60	7.98	91.1	91.3	99.4
1st Edge	15.86	16.01	17.17	86.0	86.5	100.0
2nd Flap	20.48	20.39	20.30	86.8	87.5	99.8
3rd Flap	34.24	33.76	33.95	87.7	83.2	97.5
2nd Edge	38.50	42.37	44.63	95.1	87.4	74.2

Table 4. Comparison of experimental and FEA modal results for TX-100.

Description	Frequency (Hz)			MAC Correlation (%)		
	Shell Model	Brick Model	Test (Avg.)	Shell Model-Test (Avg.)	Brick Model-Test (Avg.)	Shell Model-Brick Model
1st Flap	6.46	6.57	6.47	94.8	93.1	98.2
2nd Flap	15.59	15.63	15.15	93.9	94.0	99.9
1st Edge	25.87	25.64	25.13	95.6	96.3	99.6
3rd Flap	28.61	28.56	28.69	92.8	91.8	99.5
4th Flap	41.72	45.90	43.91	86.0	82.5	75.9

The results for the CX-100 blade show that both the shell and brick models compare favorably to the experimental results for the first five modes in both frequency and shape. The frequencies found in the analysis are within 8% of those found in the experiments, except for the 2nd edge mode of the shell model which is off by 13%. The shell and brick models compare well with one another with the exception of the 2nd edge mode.

The TX-100 analysis shows very good results for both models, with all frequencies within 5% of the experimental results. The correlations of mode shapes with the experimental results are excellent for the first 4 modes and good for the 4th flap mode. The model to model correlations are high except for the 4th flap mode.

It should be noted that for both blades, the models failed to predict the shape of the 1st torsional mode accurately. The MAC correlations between the models and the experiments were found to be lower than 70%. However, it is worthwhile to point that the shell and brick models compared somewhat favorably with each other (see Table 5), indicating that the poor results may be due to inherent problems with the models themselves. Further model refinement may make it possible to capture this mode.

Table 5. Comparison of the 1st torsion mode from the TX-100 shell and brick models.

Description	Frequency (Hz)		MAC Correlation (%)
	Shell Model	Brick Model	
CX-100 1st Torsion	57.62	55.44	95.7
TX-100 1st Torsion	70.22	65.22	88.4

For both blades, these results show that the offset-shell elements performed well in predicting the mode-shapes

and frequencies being investigated. The results found by (Laird, et al.)[9] suggested that aspect ratio played a role in the performance of offset-shell elements. Surprisingly, very high aspect ratio elements were seen to give the best results. Since the method by which these models were created imposed a lower limit on the number of circumferential element divisions, the spanwise divisions were minimized to reduce model size within acceptable shape limits. This led to a model with higher aspect ratios overall. To investigate the role this may have played in the results, another TX-100 shell model was created with four times the number of axial elements (Shell x4), thus yielding lower aspect ratios. The same analysis was run and the results are shown in Table 6. No significant difference is evident between the two models in terms of frequencies or mode shapes.

Table 6. Comparison of experimental and FEA modal results for TX-100 for shell elements with different aspect ratios.

Description	Frequency (Hz)		MAC Correlation (%)
	Shell Model	Shell x4 Model	
1st Flap	6.46	6.48	100.0
1st Edge	15.59	15.73	100.0
2nd Flap	25.87	26.01	100.0
3rd Flap	28.61	28.96	99.9
4th Flap	41.72	41.80	100.0

C. Static Analysis Results

A static loading analysis was performed on the CX-100 and TX-100 models for the purpose of comparison to the static pull experiments previously discussed. The same shell and brick models used in the modal analyses were used in a cantilevered arrangement with all nodes at the root end fixed for all degrees of freedom. The blade was loaded by distributed point loads of magnitude and location mimicking the loads and loading locations from the experiment. In the simulation, the blades were loaded to the previously mentioned test loads. The analysis assumed small rotations and deflections. Displacement data was extracted from the results for both models and is plotted along side the experimental results in Figure 22 and Figure 23. The models are seen to have accurately predicted the flapwise deflection for the CX-100 blade. The models deviate somewhat from the experimental results for the TX-100 blade from the 3 m station outward. For both blades, the shell and brick models agree very closely.

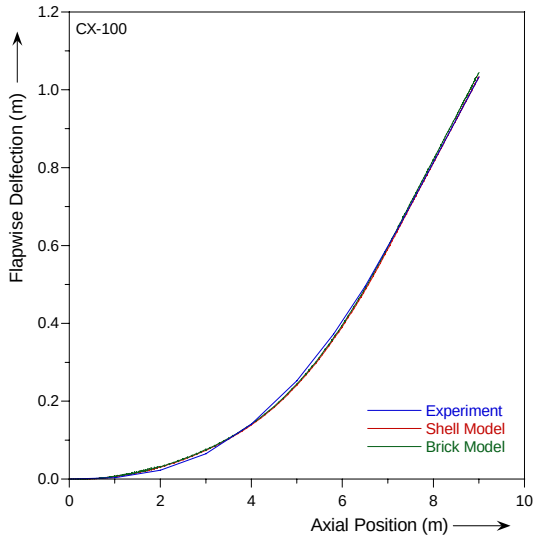

Figure 22. Comparison of CX-100 experimental and FEA deflected shape at 100% test load.

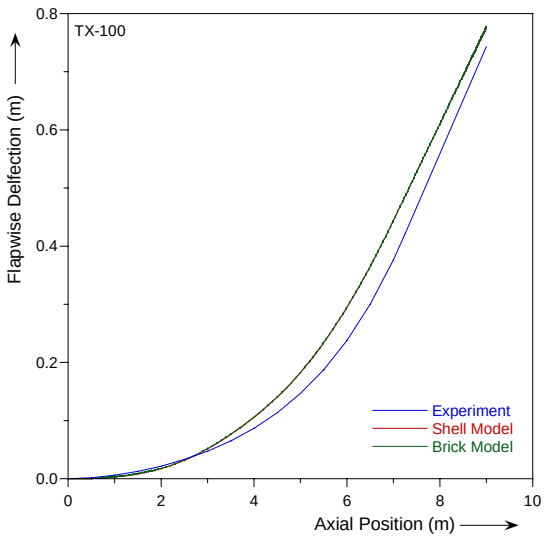

Figure 23. Comparison of TX-100 experimental and FEA deflected shape at 67% test load.

Of particular concern for the TX-100 blade was the ability of the models to predict the amount of twist present in the blade under flapwise loading. Figure 24 shows a comparison of the rotation predicted in the models to that found experimentally. The shell and brick models compare well to each other but are quite far from the experiment. As mentioned previously, it is thought that the loading apparatus used in the TX-100 experiment imposed an unknown torque on the blade which restricted twist. Further testing will need to be completed to fully understand this issue.

Finally, strain data was taken from both CX-100 and TX-100 models at locations closest to those where the strain gauges were mounted on the experimental blade specimens. Figure 25 and Figure 26 show a comparison of these strains with those measured in the experiments. Shell and brick models are seen to generally predict strains higher than measured values but are in agreement with each other. For the CX-100 blade, the shape of the strain distribution is good with the peak strains being over-predicted. For the TX-100, the models predicted stress concentrations that were not seen in the experiments. This could be due to the exact placement of individual gauges on the blade.

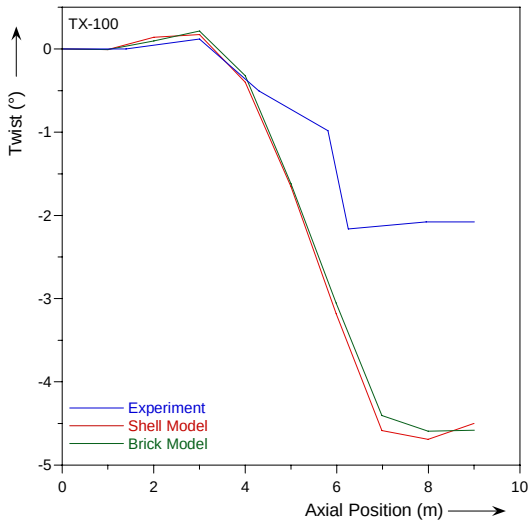

Figure 24. Comparison of TX-100 experimental and FEA twist distributions.

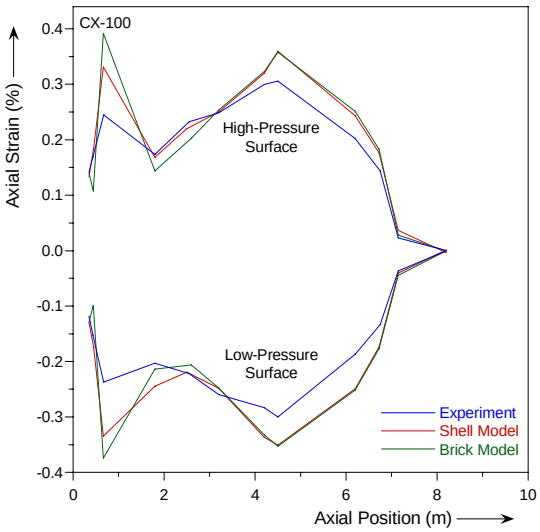

Figure 25. Comparison of CX-100 experimental and FEA strains.

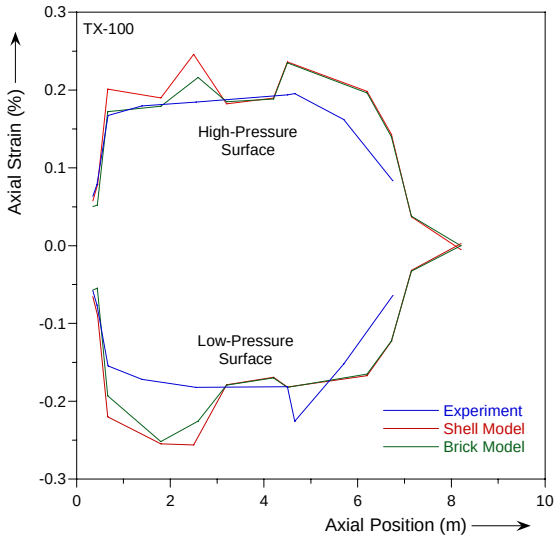

Figure 26. Comparison of TX-100 experimental and FEA strains.

VI. Conclusions

Modal and structural testing has been performed on the CX-100 and TX-100 wind turbine blades. In addition, FEA models of the two blades were made using both offset shell and solid elements. Based on a comparison of the experiments to the models, it can be concluded that both the shell and brick element models created with NuMAD accurately predicted modes under 50 Hz for both blades. The models also correctly predicted the experimentally-measured tip deflection but were slightly off in the prediction of strain values in some areas. The measured aero-elastic twist did not agree with that predicted by the models, possibly for reasons discussed earlier. The problematic issues associated with the use of offset-shell elements were not observed in the analytical results, as the shell model compared well with both the brick model and the experiments. However, further research should be completed to diagnose the cause of the inaccuracies associated with offset shell elements and the implications of these problems in the modeling of wind turbine blades and other structures.

Acknowledgments

The authors would like to acknowledge Mark Rumsey, Miguel Casias, Gregory Smith, and Sarah Reese from SNL and Scott Hughes and Jeroen van Dam from NREL for there contribution towards the research efforts outlined in this work.

References

[1] Lobitz, D. and Veers, P., "Aeroelastic Behavior of Twist-coupled HAWT Blades," *ASME/AIAA Wind Energy Symposium*, Reno, NV, 1998, pp. 75-83.

[2] Lobitz, D. and Laino, D., "Load Mitigation with Twist-coupled HAWT Blades," *ASME/AIAA Wind Energy Symposium*, Reno, NV, 1999, pp. 124-134.

[3] Lobitz, D., Laino, D., and Veers, P., "Performance of Twist-coupled Blades on Variable Speed Rotors," *ASME/AIAA Wind Energy Symposium*, Reno, NV, 2000, pp. 75-83.

[4] Wetzel, K., and Locke, J., "Uncoupled and Twist-bend Coupled Carbon-glass Blades for the LIST Turbine," Proceedings, *ASME/AIAA Wind Energy Symposium*, Reno, NV, 2004, pp. 13-23.

[5] Wetzel, K., "Utility Scale Twist-Flap Coupled Blade Design," Proceedings, *ASME/AIAA Wind Energy Symposium*, Reno, NV, 2005, pp. 382-394.

[6] Laird, D. and Ashwill, T., "Introduction to NuMAD: A Numerical Manufacturing and Design Tool," *ASME/AIAA Wind Energy Symposium*, Reno, NV, 1998, pp. 354-360.

[7] Laird, D. and Ashwill, T., "NuMAD Update: A Numerical Manufacturing and Design Tool," *ASME/AIAA Wind Energy Symposium*, Reno, NV, 1999, pp. 53-57.

[8] Laird, D., "2001: A Numerical Manufacturing and Design Tool Odyssey," *ASME/AIAA Wind Energy Symposium*, Reno, NV, 2001, pp. 20-25.

[9] Laird, D., Montoya, F., and Malcolm, D., "Finite Element Modeling of Wind Turbine Blades," *ASME/AIAA Wind Energy Symposium*, Reno, NV, 2005, pp. 9-17.

[10] Global Energy Concepts, LLC, 5729 Lakeview Drive NE, Suite 100, Kirkland, WA 98033-7340, (425) 822-9008

[11] TPI Composites, Inc., 373 Market Street, P.O. Box 328, Warren, RI 02885, (425) 247-1050

[12] Griffin, D.A., Berry, D., Zuteck, M.D., and Ashwill, T.A., "Development of Prototype Carbon-Fiberglass Wind Turbine Blades: Conventional and Twist-Coupled Designs," *AIAA/ASME Wind Energy Symposium*, Reno, NV, 2005

[13] Carne, Thomas G., and Dohrmann, Clark R., "Support Conditions, Their Effect on Measured Modal Parameters," *16th International Modal Analysis Conference*, Santa Barbara, CA, 1998, pp. 477-483,

[14] Blevins, Robert D., *Formulas for Natural Frequency and Mode Shape*, Kreiger, Malabar, Florida, 1995.

[15] ANSYS, Inc., 201 Johnson Road, Houston, PA 15342-1300, (412) 746-3304